JOURNAL OF SYNCHROTRON RADIATION

ISSN 1600-5775

Received 20 November 2018
Accepted 4 May 2019

Edited by Y. Amemiya, University of Tokyo, Japan

Keywords: X-ray speckle visibility spectroscopy (XSVS); X-ray photon correlation spectroscopy (XPCS); X-ray coherence; speckle; dynamics; photon-counting detectors; photon-counting statistics.

Supporting information: this article has supporting information at journals.iucr.org/s

Implications of disturbed photon-counting statistics of Eiger detectors for X-ray speckle visibility experiments

Johannes Möller,[a]* Mario Reiser,[a,b] Jörg Hallmann,[a] Ulrike Boesenberg,[a] Alexey Zozulya,[a] Hendrik Rahmann,[b] Anna-Lena Becker,[b] Fabian Westermeier,[c] Thomas Zinn,[d] Federico Zontone,[d] Christian Gutt[b] and Anders Madsen[a]

[a]European X-ray Free Electron Laser Facility, Holzkoppel 4, D-22869 Schenefeld, Germany, [b]Department Physik, University Siegen, D-57072 Siegen, Germany, [c]Deutsches Elektronen Synchrotron DESY, D-22607 Hamburg, Germany, and [d]ESRF – The European Synchrotron, F-38043 Grenoble, France. *Correspondence e-mail: johannes.moeller@xfel.eu

This paper reports on coherent scattering experiments in the low-count regime with less than one photon per pixel per acquisition on average, conducted with two detectors based on the Eiger single-photon-counting chip. The obtained photon-count distributions show systematic deviations from the expected Poisson–gamma distribution, which result in a strong overestimation of the measured speckle contrast. It is shown that these deviations originate from an artificial increase of double-photon events, which is proportional to the detected intensity and inversely proportional to the exposure time. The observed miscounting effect may have important implications for new coherent scattering experiments emerging with the advent of high-brilliance X-ray sources. Different correction schemes are discussed in order to obtain the correct photon distributions from the data. A successful correction is demonstrated with the measurement of Brownian motion from colloidal particles using X-ray speckle visibility spectroscopy.

1. Introduction

Free-electron lasers (FELs) and diffraction-limited storage rings (DLSRs) are new-generation X-ray sources, which offer increased brilliance and subsequently higher coherent flux in the hard X-ray regime than has been previously available. In particular, X-ray photon correlation spectroscopy (XPCS) will profit from these superior coherent properties (Grübel *et al.*, 2007; Shpyrko, 2014), as an increase in coherent flux by a factor of 100 results in 10 000 times shorter timescales being accessible with the same signal-to-noise ratio (Falus *et al.*, 2006). This will expand the scope of XPCS to new applications at shorter timescales and smaller length scales, bridging the gap to frequency-domain techniques such as inelastic X-ray scattering, but might also call for different experimental realizations due to the challenges emerging with the faster repetition rates and higher X-ray intensities.

Because of the limited coherent flux and low scattering cross section of X-rays, XPCS experiments are typically being performed as multi-speckle acquisitions with 2D area detectors, which restricts the accessible timescales by the limited frame rate of such detectors. The increasing photon flux of modern synchrotron facilities as well as the continuous development of faster 2D detectors have pushed the limit of XPCS to µs timescales in recent years (Johnson *et al.*, 2012; Zhang *et al.*, 2016, 2018). With the advent of X-ray FELs

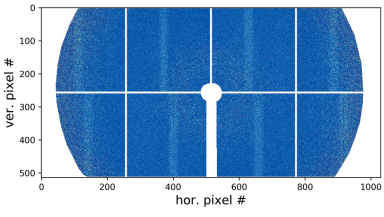

(XFELs), the first sequential XPCS measurements have been performed using the repetition rates of the sources (Carnis *et al.*, 2014; Lehmkühler *et al.*, 2015). Based on the expected increase in coherent flux envisaged for DLSRs, and the subsequent accessibility of shorter timescales, the pulsed nature of synchrotrons might in the future also be employed in XPCS experiments (Shpyrko, 2014). Making use of the inherent time resolution offered by the repetition rate and pulse length of new-generation X-ray sources calls for faster detectors or new strategies for probing sample dynamics with coherent X-rays (Grübel *et al.*, 2007; Shpyrko, 2014).

This purpose can be served by speckle visibility spectroscopy (SVS), which is a coherent scattering technique aiming at the observation of dynamics by evaluating the statistical properties of speckle patterns taken with different exposure times. It was first introduced in laser-light scattering (Bandyopadhyay *et al.*, 2005) and later extended to X-rays (XSVS) (Gutt *et al.*, 2009; Hruszkewycz *et al.*, 2012; Inoue *et al.*, 2012; Li *et al.*, 2014). By relating the speckle contrast to the experimental integration time, the dynamics of a sample can be obtained. The longer the exposure time of a measurement compared with the internal dynamics of the sample, the more 'blurred' the resulting speckle pattern appears and a loss in contrast can be observed.

The advantage of XSVS, compared with sequential XPCS, is the fact that it offers access to timescales faster than the frame rate of the detector, since only the information content within single images is evaluated. Therefore, each exposure on the sample can also be performed at a new spot, which was shown to be beneficial for studying radiation-sensitive samples (Verwohlt *et al.*, 2018). Recently, it has also been demonstrated that XSVS is a valuable tool to access ultra-fast timescales by varying the pulse length of an XFEL (Perakis *et al.*, 2018) or by double-pulse experiments (Seaberg *et al.*, 2017; Roseker *et al.*, 2018). In this case, the time delay between two X-ray pulses is varied, and the contrast of the summed scattering image is evaluated as a function of time difference between these two pulses. Numerous experimental realizations have been developed for double-pulse experiments, either by using specific modes of the electron accelerator (Decker *et al.*, 2010; Seaberg *et al.*, 2017; Sun *et al.*, 2018) or by split-and-delay schemes of the X-ray optics (Roseker *et al.*, 2009, 2011, 2018; David *et al.*, 2015; Lu *et al.*, 2016, 2018; Osaka *et al.*, 2016, 2017; Sakamoto *et al.*, 2017; Zhu *et al.*, 2017; Hirano *et al.*, 2018). The resulting timescales range between fs and ns, making it impossible to resolve two pulses with multi-pixel area detectors. Therefore, such experiments strongly rely on the use of XSVS.

XSVS experiments at synchrotrons and XFELs, compared with laser-light SVS, have in common that typically very low intensities per pixel per exposure are encountered, which complicates the analysis and robustness of the method (Hruszkewycz *et al.*, 2012; Inoue *et al.*, 2012; Li *et al.*, 2014; Verwohlt *et al.*, 2018). At low count rates, the determination of the speckle contrast is not only dominated by shot noise but is also very sensitive to detector artifacts which may alter the photon statistics and render a contrast analysis challenging.

The Eiger photon-counting detector, and its predecessor Pilatus, are well-established detectors, widely used for various applications like protein crystallography, small-angle X-ray scattering or photon correlation spectroscopy (Westermeier *et al.*, 2009; Hoshino *et al.*, 2012; Johnson *et al.*, 2012; Casanas *et al.*, 2016). In order to quantify the XSVS performance, we set out to measure detected photon-count distributions for two different versions of the Eiger detector. We find systematic deviations from the expected photon-count statistics, which we relate to an artificial increase in two-photon counts. The reported miscounting effect is not detectable in conventional X-ray scattering experiments, which illustrates that XSVS can also serve as a cutting-edge tool to study the performance of area detectors.

2. X-ray speckle visibility spectroscopy

XSVS and XPCS are both experimental techniques used to obtain the intermediate scattering function (ISF) $g_1(\mathbf{q}, t)$ and therefore information about the dynamics of a sample. In the case of XPCS, a sequential acquisition of speckle pattern is used to calculate the autocorrelation function of the scattered intensity $I(\mathbf{q}, \tau)$ as

$$g_2(\mathbf{q}, t) = \frac{\langle I(\mathbf{q}, \tau)\, I(\mathbf{q}, \tau + t)\rangle}{\langle I(\mathbf{q})\rangle^2}, \tag{1}$$

with the absolute value $|\mathbf{q}| = q = 4\pi \sin(\theta/2)/\lambda$ being the scattering vector, depending on the wavelength λ and the scattering angle θ. The time delay between two consecutive time frames is denoted t, and $\langle \ldots \rangle$ is the ensemble average over all equivalent delay times t and pixels within a certain q-range. The ISF follows from this via the Siegert relation

$$g_2(q, t) = 1 + \beta_0 \left| g_1(q, t) \right|^2, \tag{2}$$

with β_0 being the speckle contrast. However, the scattering intensity $I(q, \tau)$ measured at a time τ cannot be measured with infinite time resolution. This means that in reality the integrated intensity of a single frame with exposure time T is measured, given by

$$\bar{I}(q, \tau, T) = \int_{\tau}^{\tau+T} I(q, \tau')\, \mathrm{d}\tau'. \tag{3}$$

In practice, the influence of the exposure time on the experiment can be neglected, as long as T is shorter than the typical timescales of the sample's dynamics. However, if T increases towards these timescales, a decrease in contrast is observed due to fluctuations of the speckle pattern during detector exposure. The decay of speckle contrast is connected to the ISF (Bandyopadhyay *et al.*, 2005) as

$$\beta(q, T) = 2\frac{\beta_0}{T} \int_0^T (1 - t/T) \left| g_1(q, t) \right|^2 \mathrm{d}t. \tag{4}$$

Therefore, one can probe the ISF from a series of single frame acquisitions, where the exposure time T is varied. The ISF of

a system exhibiting diffusive motion is described by a single exponential decay

$$\left|g_1(q,t)\right|^2 = \exp[-2t/\tau(q)], \tag{5}$$

where the correlation time $\tau(q)$ is given by $\tau(q) = 1/(Dq^2)$, with the diffusion coefficient D. For this case, equation (4) can be solved analytically (Bandyopadhyay *et al.*, 2005) as

$$\beta(q,T) = \beta_0 \frac{\exp[-2T/\tau(q)] - 1 + 2T/\tau(q)}{2[T/\tau(q)]^2}. \tag{6}$$

This approach is termed speckle visibility spectroscopy and was first introduced for laser-light scattering, where the contrast β can be calculated from the normalized variance of intensities within a q-bin (Bandyopadhyay *et al.*, 2005). This is however only valid for intense beam conditions, where shot noise is negligible and the photon statistics follow the gamma distribution.

2.1. Poisson–gamma distribution

For the lower intensities typically encountered in coherent X-ray scattering experiments, the Poisson-distributed, discrete nature of the photons registered by a pixel has to be taken into account. Therefore, the probability P of k photons being registered within one speckle is given by a convolution of the gamma and the Poisson distribution (Goodman, 1985). This results in the negative-binomial distribution, also known as the Poisson–gamma (PG) distribution,

$$P(k) = \frac{\Gamma(M+k)}{\Gamma(M)\Gamma(k+1)} \left(1 + \frac{M}{\langle k\rangle}\right)^{-k} \left(1 + \frac{\langle k\rangle}{M}\right)^{-M}, \tag{7}$$

with M being the number of coherent modes, which is related to the speckle contrast as $\beta = 1/M$ and the average number of photons per pixel $\langle k\rangle$. Hence, the speckle contrast can be obtained from the probabilities of pixels within an ensemble measuring $k = 0, 1, 2\ldots$ photons. Different relations for the determination of the speckle contrast can be derived from equation (7). For example, with

$$P(k+1) = P(k) \frac{M+k}{k+1} \left(1 + \frac{M}{\langle k\rangle}\right)^{-1}, \tag{8}$$

the contrast β can be obtained only from the ratio of $P(0)$ and $P(1)$ as

$$\beta_{01} = \frac{P(0)}{P(1)} - \frac{1}{\langle k\rangle}. \tag{9}$$

It can easily be seen that the occurrence of two-photon counts is needed for the determination of β. Otherwise, $P(2) = 0$ and $P(1) = \langle k\rangle$, which would result in $\beta_{01} = -1$. Therefore, a reliable determination of $P(2)$ is crucial for XSVS, which can be difficult in the very low count regime.

The dependence of $P(2)$ on β can be simplified in this regime by a Taylor expansion for $\langle k\rangle \ll 1$:

$$P(2) = \frac{1}{2}(1+\beta)\langle k\rangle^2 - \frac{1}{2}(1+3\beta+2\beta^2)\langle k\rangle^3 + O(\langle k\rangle^4). \tag{10}$$

This results in

$$\beta \simeq \frac{2P(2)}{\langle k\rangle^2} - 1, \tag{11}$$

showing that $\beta + 1$ is proportional to $P(2)$ at low count numbers. From this relation, the error for determining a speckle contrast can be calculated (Hruszkewycz *et al.*, 2012) as

$$\Delta\beta = \frac{1}{\langle k\rangle} \left[\frac{2(\beta+1)}{N_{\rm pix} N_{\rm frames}}\right]^{1/2}, \tag{12}$$

with $N_{\rm pix}$ being the number of pixels and $N_{\rm frames}$ the number of frames in the ensemble average.

3. Experiments

The experiments were conducted with two different detectors, both based on the Eiger single-photon-counting chip. One Eiger module consists of 2 by 4 chips with an active area of 38 mm × 77 mm. Each of the chips has 256 × 256 square pixels with a width of 75 µm (Dinapoli *et al.*, 2011; Radicci *et al.*, 2012). With variable depths of the pixel counter, 4, 8 or 12 bits, frame rates up to 22, 12 and 8 kHz can be achieved, respectively (Johnson *et al.*, 2014). A specific feature of the Eiger chip is the parallel read-out of pixels while already acquiring a subsequent exposure, due to an on-pixel storing buffer (Radicci *et al.*, 2012). The reset of the main counter allows the start of a new exposure while the buffer information is read out, resulting in a short deadtime between frames of $t_{\rm dead} \simeq 3$ µs (Radicci *et al.*, 2012). Mega-pixel cameras are commercially available, based on assemblies of single modules.

In this work, we will compare the results from a single Eiger module (PSI Eiger 500k, up to 22 kHz) and a commercial 4M version consisting of eight single modules (Dectris Eiger 4M, 750 Hz). The single module Eiger 500k detector, provided by the Paul Scherrer Institute (PSI), Switzerland, was used at the beamlines ID02 and ID10, ESRF, Grenoble, France (Chushkin *et al.*, 2014; Möller *et al.*, 2016; Narayanan *et al.*, 2018; Zinn *et al.*, 2018). At beamline ID02, the sample-to-detector distance was 31 m with a photon energy of 12.4 keV. The Dectris Eiger 4M was used at beamline P10, Petra III, DESY, Hamburg, Germany (Zozulya *et al.*, 2012). The sample-to-detector distance was 21 m with a photon energy of 8 keV. The long sample-to-detector distances offered by the two USAXS (ultra small angle X-ray scattering) setups at ID02 and P10 allow a rather homogeneous illumination of the detector by photons scattered from a static sample. Therefore, a large number of pixels could be used for ensemble averaging, which is crucial to obtain good statistics. A shorter sample-to-detector distance of 5.3 m was used at beamline ID10 at nearly the same photon energy (8.1 keV) in order to increase the average number of photon counts per pixel. At all beamlines, the speckle contrast was $\beta > 20\%$.

In order to characterize the dependence of the measured speckle contrast on the exposure time and mean intensity, different reference samples (vycor glass, aerogel) were

measured with various exposure times T and beam attenuations. As both samples are static, no dependence on $\langle k \rangle$ and T should be observable. Additionally, the dependencies of the obtained photon statistics on the detector pixel threshold and the read-out mode were investigated. The dynamic XSVS measurements were conducted at beamline ID10, on charged stabilized silica particles in a water/glycerol mixture. For comparison, regular XPCS measurements were performed on this sample as well.

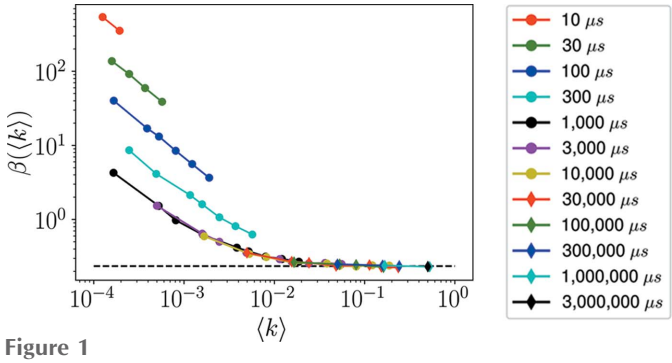

Figure 1
Calculated speckle contrast of a static aerogel sample as a function of mean photon count per pixel $\langle k \rangle$. The contrast is calculated following equation (9). The overestimation of the speckle contrast increases with decreasing exposure time and intensity. The black dashed line corresponds to the expected value $\beta_0 = 0.23$.

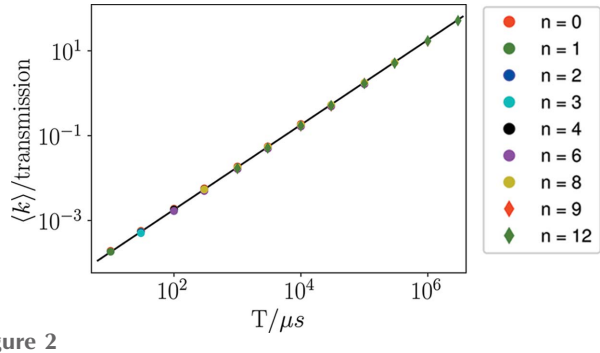

Figure 2
Transmission corrected mean intensities shown as a function of exposure time T, with n being the number of used absorber elements. The black line shows the linear relation between measured intensity and exposure time, corresponding to 18 counts per second per pixel of the unattenuated beam.

4. XSVS on a static sample

XSVS measurements were performed on a static aerogel sample using the Dectris 4M detector at the coherence beamline P10 of the PETRA III synchrotron source, DESY. The exposure time was varied from 10 µs up to 3 s and different numbers n of 25 µm-thick Si attenuators were used. With this, the incoming intensity could be reduced by a factor 0.68^n, with n ranging from 0 to 12. This resulted in mean intensities $\langle k \rangle = 10^{-4}$–$10^{0}$ photons per pixel per exposure. The mean intensity $\langle k \rangle$ and the probabilities $P(k)$ were calculated for each single acquisition, and averaged for each exposure time and attenuator setting. Overall, up to 1000 frames for the shortest exposure time were averaged over 2.8 Mpixel. From this, the mean contrast β is calculated via equation (9). The results are shown in Fig. 1 as a function of mean intensity $\langle k \rangle$.

The black dashed line corresponds to the expected value $\beta_0 = 0.23$. As the measured sample is static, this value should be similar for all exposure times and attenuator settings. However, as can be seen in Fig. 1, it is obtained for higher intensities only. Towards lower count rates, a systematic overestimation of the contrast β can be found. For exposure times of 1 ms and longer, the measured values superimpose on a single line, which increases with decreasing $\langle k \rangle$. For even shorter exposure times, an additional increase in β with decreasing exposure time can be observed. For all exposure times T, however, unphysical contrast values of $\beta \gg 1$ are observed when the mean intensity $\langle k \rangle$ decreases.

In Fig. 2, the $\langle k \rangle$ values of Fig. 1 are shown as a function of exposure time T, normalized by the transmission of the different absorbers. It is evident that the overall intensity measured by the detector scales as expected over a wide range of intensities. This means that the problem illustrated in Fig. 1 would most probably not be noticed in a conventional scattering experiment, but it can lead to a large error in coherent scattering experiments, where the speckle contrast is the important quantity to be measured.

4.1. Excess of two-photon events

In order to investigate the origin of this effect, we examine the distribution of photon counts per pixel. Fig. 3 displays the measured probability $P(k)$ for a pixel counting k = 0, 1 or 2

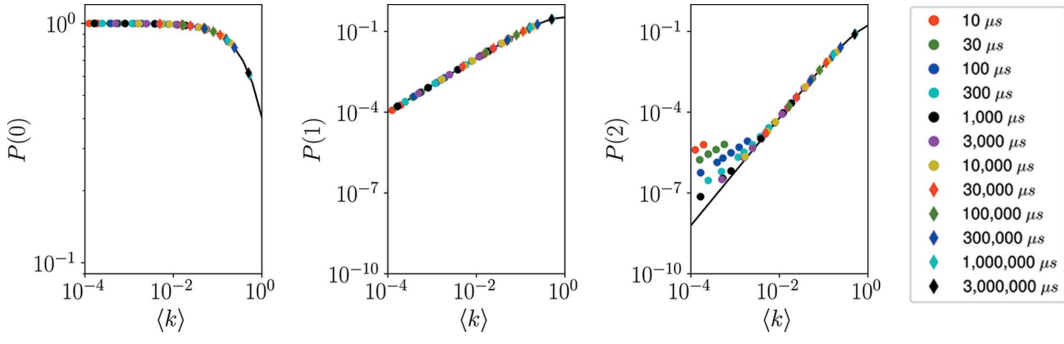

Figure 3
Distribution of photon-count probabilities as a function of number of photons per pixel $\langle k \rangle$, measured with the Dectris Eiger 4M at beamline P10. The corresponding figure for the PSI Eiger 500k used at beamline ID02 can be found in the supporting information. In black, the expected Poisson–gamma distribution is plotted for $\beta = 0.23$.

photons, plotted as a function of mean number of photons per pixel $\langle k \rangle$. These are obtained from the same data as used in Fig. 1. The probabilities for 0 and 1 photon events seem to follow the PG distribution well (black line). In the case of two-photon events, however, systematic deviations from the PG distribution are visible. For the lowest intensities of $\langle k \rangle \simeq 10^{-4}$, the number of pixels counting two photons is increased by about three orders of magnitude. This means that double-photon events make up about 7% of the overall intensity at $T = 10$ µs, even though according to the PG distribution close to 100% of the intensity should be registered as single-photon events [$P(1) \simeq 10^{-4}$, $P(2) \simeq 10^{-8}$]. It can easily be seen from the relation between $P(2)$ and β at low count rates [equation (11)] that such an increase in $P(2)$ leads to contrast values which exceed physically possible values by orders of magnitude.

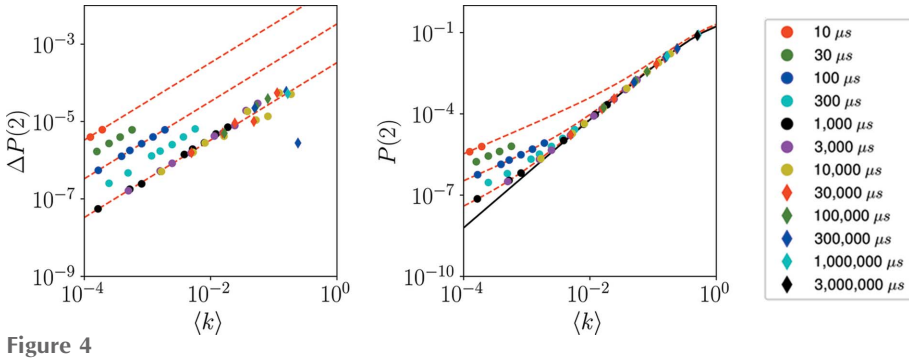

Figure 4
(Left) Differences between measured and expected number of double-photon counts, calculated by equation (13). The red lines follow the linear relation in equation (14), with $\kappa(T = 10\ \text{ms}) \simeq 0.00033$, $\kappa(T = 100\ \mu\text{s}) = 0.0033$ and $\kappa(T = 10\ \mu\text{s}) = 0.033$. (Right) Raw data of $P(2)$ together with equation (14) added to the Poisson–gamma distribution (red lines).

We further investigate this by taking the difference between expected [$P(k = 2)$, black line] and measured [$P_{\text{exp}}(k = 2)$, data points] probabilities, plotted in Fig. 4 (left), as

$$\Delta P(k) = P_{\text{exp}}(k) - P(k, \langle k \rangle, \beta). \tag{13}$$

The different behavior for exposure times below and above 1 ms can also be seen in $\Delta P(k)$. For exposure times of 1 ms and above, the data superimpose, whereas they depend on T for $T \leq 1$ ms. Additionally, it is evident that, for each exposure time, the number of extra double-photon events depends linearly on $\langle k \rangle$. This is displayed in Fig. 4 (left) as red dashed lines, following

$$\Delta P(2) = \kappa(T)\langle k \rangle. \tag{14}$$

where κ is a T-dependent scattering factor. For $T \geq 1$ ms, we find $\kappa \simeq 0.00033$. For shorter exposure times, the factor κ increases proportionally with the decreasing exposure times: $\kappa(T = 100\ \mu\text{s}) = 0.0033$; $\kappa(T = 10\ \mu\text{s}) = 0.033$. The factor κ is hence

$$\kappa(T) = \begin{cases} 0.33\ \mu\text{s}/T & \text{for } T < 1\ \text{ms}, \\ 0.33\ \mu\text{s}/1000\ \mu s & \text{for } T \geq 1\ \text{ms}. \end{cases} \tag{15}$$

Therefore, the increase in $P(2)$ is proportional to the impinging intensity on the detector, suggesting that a certain fraction of the intensity is falsely converted into double-photon events. The factor $\kappa(T)$ describes the probability of this miscounting happening. As the number of double-photon events can be orders of magnitude smaller than that of single-photon events, even a very small conversion probability from single- to double-photon events can impose a large difference on $P(2)$. Therefore, this miscounting effect has a stronger influence on the measured speckle contrast the more $P(1)$ and $P(2)$ diverge, *i.e.* the smaller $\langle k \rangle$ gets.

Additionally, the conversion probability $\kappa(T)$ increases when decreasing the exposure time T below 1 ms. Two resulting regimes above and below 1 ms exposure time can be identified. The difference in behavior for the two regimes might stem from the auto-summation performed by the detector. Above a certain exposure time, the detector acquires a series of shorter frames, which are summed and transferred as a single image. Therefore, all data acquired with exposure times $T > 1$ ms show the same miscounting characteristics as $T = 1$ ms.

In the next step, we will evaluate how the measured speckle contrast can be connected to the real speckle contrast β_0. We find that the resulting increase in β, previously shown in Fig. 1, can be described by the following expression:

$$\beta(T) = \beta_0 + \frac{2\kappa(T)}{\langle k \rangle}, \tag{16}$$

which is displayed in Fig. 5 (left) as red lines, with $\kappa(T)$ given in equation (15).

Inserting equation (16) into the expression for $\beta[P(2)]$ at small $\langle k \rangle$ [equation (11)], we obtain

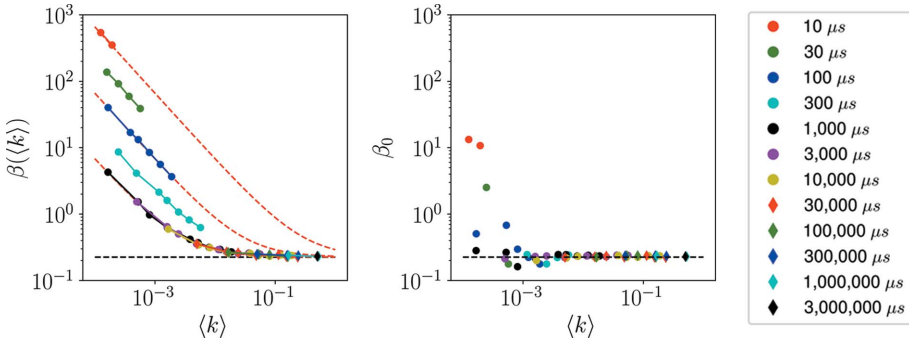

Figure 5
(Left) Speckle contrast β calculated for different exposure times and attenuator setting, already shown in Fig. 1. The additional red lines follow equation (16) with the previously reported values of κ in equation (15). (Right) Corrected speckle contrast β_0, obtained from equation (16).

$$\beta_0 \simeq \frac{2[P(2) - \kappa(T)\langle k\rangle]}{\langle k\rangle^2} - 1. \qquad (17)$$

Comparing with equation (11), one can see that this results in the same correction for $P(2)$ as in equation (14). Therefore, we use equation (16) to obtain the corrected speckle contrast β_0.

The resulting speckle contrasts β_0 are shown in Fig. 5 (right). The much reduced contrast has no systematic dependence on T and $\langle k\rangle$ anymore. Stronger deviations from the expected contrast values can be observed at the lowest intensities, below $\sim 5 \times 10^{-4}$ photons per pixel per exposure. At this intensity, the statistical uncertainty in determining the speckle contrast can be estimated as [equation (12)] $\Delta\beta < 0.002$. We account for the apparently larger influence of shot noise on the determination of β by the larger uncertainty in determining $P(2)$; this is due to the artificial increase in two-photon events, which would require even more repetitions or more pixels in the ensemble average for a reliable determination of the speckle contrast. We will show in Section 5 that the derived correction can be used to obtain the Brownian dynamics of colloidal particles using XSVS. First, the origin of the additional double-photon events will be further discussed in the following sections.

4.2. Conversion schemes

We established that a certain fraction of the detected intensity is converted into double-photon events and that the probability of this conversion is given by the factor $\kappa(T)$. Two simple possibilities for such conversions are sketched in Fig. 6. Case I assumes that a single-photon pixel is converted into a double-photon event, falsely adding one photon. Case II corresponds to two pixels which should both register one photon, but are converted into one pixel registering two photons and a pixel with 0 photons. This corresponds to a cross talk or merging effect.

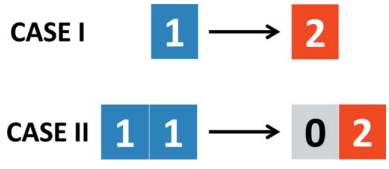

Figure 6
Two different cases which are evaluated to explain the distortion of the photon-count distributions.

Taking into account the conversion probability κ, the undisturbed photon-count probabilities are given in Table 1.

Table 1
Different schemes to correct the measured photon-count distributions following the two cases sketched in Fig. 6.

Case I	Case II
$\langle k\rangle = \langle k\rangle_{\rm exp} - \kappa(t)P(1)_{\rm exp}$	$\langle k\rangle = \langle k\rangle_{\rm exp}$
$P(0) = P(0)_{\rm exp}$	$P(0) = P(0)_{\rm exp} - \kappa(t)P(1)_{\rm exp}$
$P(1) = P(1)_{\rm exp} + \kappa(t)P(1)_{\rm exp}$	$P(1) = P(1)_{\rm exp} + 2\kappa(t)P(1)_{\rm exp}$
$P(2) = P(2)_{\rm exp} - \kappa(t)P(1)_{\rm exp}$	$P(2) = P(2)_{\rm exp} - \kappa(t)P(1)_{\rm exp}$

First, we use these corrections to calculate the corrected speckle contrast β_0, which is displayed in Fig. 7. Additionally, equation (16) is used for comparison.

As can be seen, the resulting contrast values β_0 closely resemble each other for all three different correction schemes. This can be understood by the fact that the speckle contrast in this low counting regime is mainly governed by the occurrence of two-photon events, *i.e.* $P(2)$. As this value is corrected effectively the same way for all three correction schemes, these are basically indistinguishable when only the contrast values β_0 are evaluated.

Therefore, we further verify these models against the measured photon statistics, already shown in Fig. 3. For this, the differences between the expected and measured photon probabilities are calculated following equation (13) and displayed in Fig. 8.

It becomes evident that not only the values of $P(2)$ show systematic deviations but that $P(0)$ and $P(1)$ are disturbed in a very similar way. The following observations can be made from these data:

(i) Too many pixels register 2 and 0 photons, too few are counting 1 photon, as $\Delta P(k=0)$ and $\Delta P(k=2) > 0$; $\Delta P(k=1) < 0$.

(ii) For each exposure time and each k, $\Delta P(k)$ is proportional to $\langle k\rangle$.

(iii) The absolute values of the excess 0- and 2-photon events are nearly equal for all exposure times, $\Delta P(k=0) \simeq \Delta P(k=2)$.

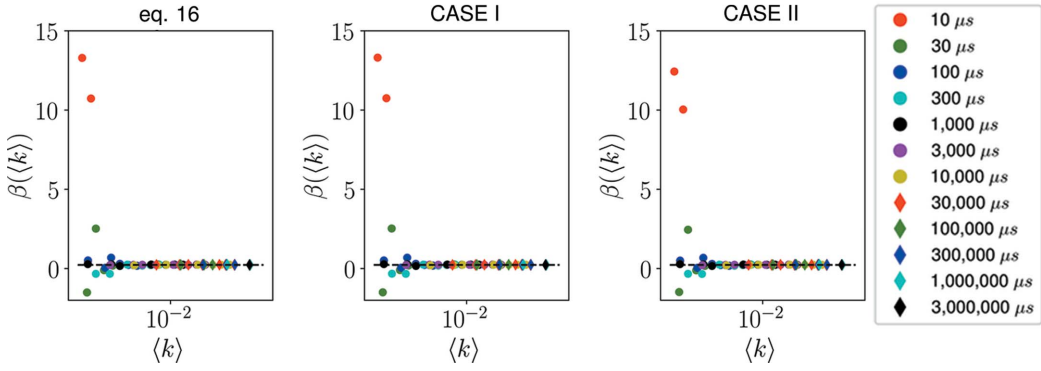

Figure 7
Corrected speckle contrast β_0, obtained by using (left) equation (16), (middle) case I and (right) case II.

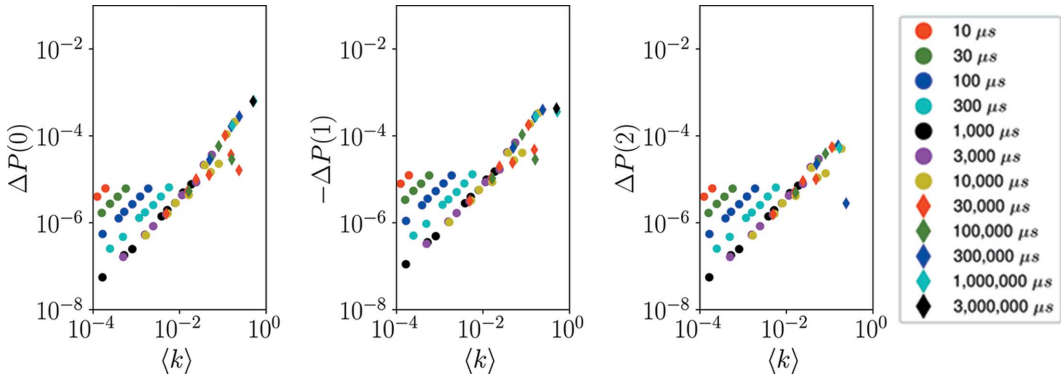

Figure 8
Difference between expected and measured photon-count probabilities for k = 0, 1 and 2 photons, calculated as in equation (13).

(iv) The excess 0- and 2-photon events add up to account for the missing 1-photon events, $\Delta P(k=0) + \Delta P(k=2) \simeq -\Delta P(k=1)$.

The latter two points are additionally illustrated in Fig. 9.

These findings strongly support case II, where two 1-photon events are converted into a single 2-photon event and a single 0-photon event. Therefore, 2κ of the 1-photon events $P(1)$ are removed, and correspondingly these are added evenly to $P(2)$ and $P(0)$.

Additionally, one can use this model to calculate the resulting miscounting probability κ directly from the data, by solving the equations displayed in Table 1 for κ as

$$\kappa = \frac{\langle k \rangle [P(0)_{\rm exp} - \beta_0 P(1)_{\rm exp}] - P(1)_{\rm exp}}{P(1)_{\rm exp}(2\beta_0 \langle k \rangle + \langle k \rangle + 2)}. \qquad (18)$$

The resulting miscounting probabilities are displayed in Fig. 10 as a function of exposure time T. The absolute values as well as the dependence on the exposure times are in line with previous observations [black line, equation (15)].

In summary, case II explains the observed deviations of $P(k)$ almost perfectly. Therefore, we assume that the detector combines with a certain probability two photons, which should be registered in separate pixels, into a double-photon count. By this, the absolute number of photons detected stays the same (compare Fig. 2), but the distribution of $P(k)$ is distorted. It should be noted that a small increase in counts per second for shorter exposure times below 1 ms can be observed (see Fig. S2 in the supporting information), as would be predicted by case I. However, this increase shows a step-like dependence on T, which cannot be explained by either of the two schemes. Additionally, no feature of the previously discussed miscounting behaviors shows such a step-like dependence on T around T = 1 ms. Therefore, we cannot conclude that this slight increase in intensity is related to the artificial increase in speckle contrast reported here.

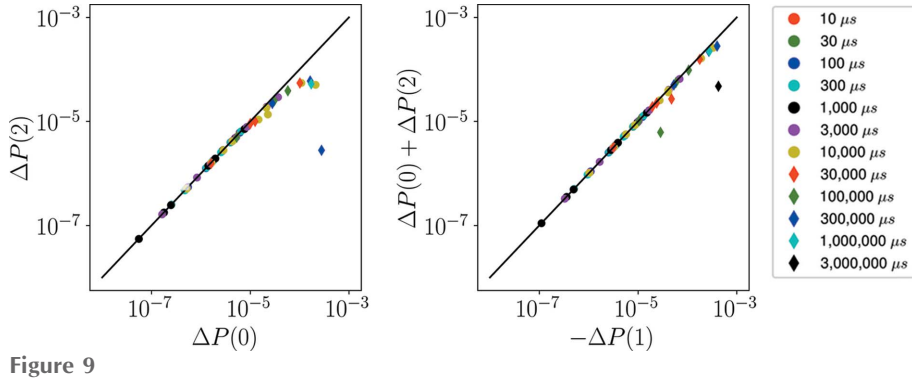

Figure 9
Linear relations between $\Delta P(k)$ for different k. (Left) $\Delta P(k=0) \simeq \Delta P(k=2)$, (right) $\Delta P(k=0) + \Delta P(k=2) \simeq -\Delta P(k=1)$. The black lines serve as a guide to the eye, following $x = y$.

4.3. Spatial distribution of double-photon events

In this section, the spatial distribution of the artificial double-photon counts on the detector is evaluated. For this, we will focus on data measured at T = 10 µs only, as these have the highest conversion probability and nearly all detected double-photons events can be assumed to be artificially

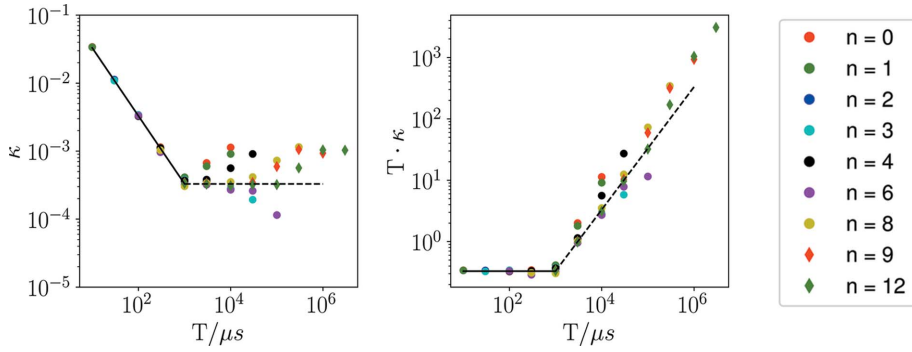

Figure 10
Dependence of the correction parameter κ on the exposure time T. The black and black dashed line correspond to equation (15).

produced. We point out that all shown data up to here were taken with the Dectris Eiger 4M. The corresponding plots with the PSI 500k version are shown in the supporting information, measured at beamline ID02 at the ESRF. Qualitatively, the same distortion of the counting statistics was found for this detector with slightly different absolute values of κ. As previously reported, we obtained $\kappa = 0.33\ \mu s/T$ at beamline P10 with the Dectris Eiger 4M and $\kappa = 0.34\ \mu s/T$ at beamline ID02 with the PSI Eiger 500k. For the following data, measured at beamline ID10 with the same Eiger module as at ID02, we obtain a slightly higher $\kappa = 0.39\ \mu s/T$. This can most likely be explained by the different photon energy and detector threshold settings ($E_{ID02} = 12.4$ keV; $E_{ID10} = 8.1$ keV). The dependence of κ on the detector threshold is depicted in the supporting information.

In Fig. 11 (top), the scattering intensity of a vycor reference sample is shown, measured at beamline ID10, ESRF, with the PSI Eiger 500k. In total 60 000 single acquisitions have been summed to obtain sufficient statistics on the single pixel level. Areas of the detector which are shadowed by the flight tube or the beamstop as well as the pixels on the border of the eight single chips have been masked. The isotropic, ring-shaped scattering intensity, $I(q)$, of the vycor glass can be clearly seen.

In Fig. 11 (bottom), only the fraction of the scattering intensity is shown that originates from double-photon events. Two main observations can be made. First, the isotropic ring structure of $I(q)$ is not visible. In fact quite the opposite, in that each pixel shows roughly the same fraction of double-photon events per incoming intensity. This additionally illustrates the previously reported observation that a constant fraction of the incoming intensity is falsely converted into double-photon events. The second observable feature is the vertical stripes, which are present and similar for each detector chip. In this region, a slightly higher fraction of the incoming intensity is converted into artificial double-photon events. Interestingly, these stripes seem to be at the same position for each of the eight chips, with respect to the underlying read-out electronics of the chip located at each of the long detector boarders, so that on the bottom half of the detector the chips are rotated by 180° with respect to the top half (Dinapoli *et al.*, 2011).

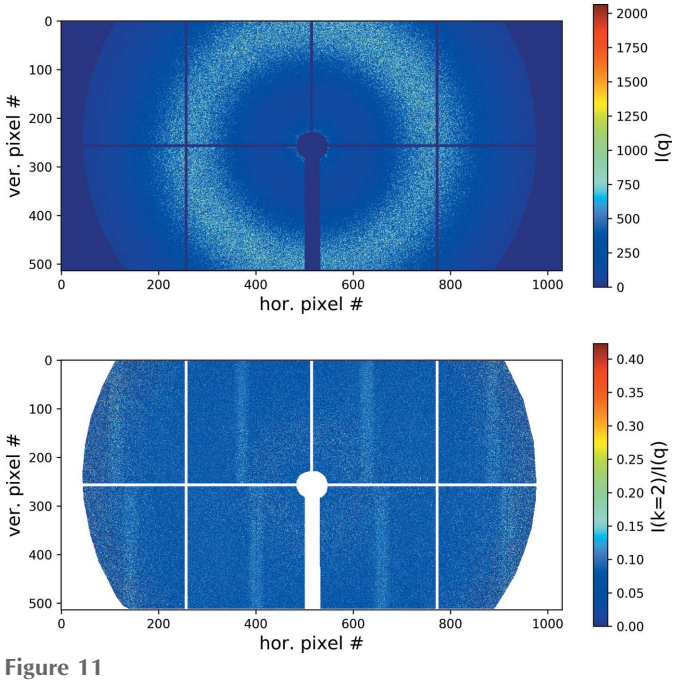

Figure 11
(Top) Summed scattering intensity $I(q)$ of 60 000 single scattering acquisitions of vycor, each with an exposure time of 10 µs. (Bottom) Fraction of the measured intensity, which is registered as double-photon counts, calculated for each pixel separately.

The fixed locations of the stripes for each chip are additionally illustrated in Fig. 12, where the average of each vertical pixel line is shown as a function of horizontal position. The detector is divided into a top and a bottom half, whereas the horizontal direction of the top detector half is flipped. The double-sized pixels on the chip borders have been marked by vertical red lines and the middle of each chip by a vertical black line. One can clearly observe an additional increase in double-photon events in a narrow region, for each chip starting at the middle of the chip and lasting for 32 pixels. It should be noted that the artificial increase in double-photon events is not limited to the stripe regions, but the conversion probability in this region is even higher than for the rest of the detector. The baseline in Fig. 12, however, corresponds quite well to the value $2\kappa(10\ \mu s) \simeq 0.078$, which is the fraction of intensity which is converted from one-photon events to two-photon events (see for example case II in Table 1). It is evident, however, that the conversion probability changes as a function of horizontal position on the detector.

In fact, the reported conversion of one-photon events into two-photon events is measured with both types of Eiger detectors, with roughly the same average conversion probabilities. However, the configuration at P10, where the Dectris Eiger 4M is 22 m from the sample position, gave much less intensity per pixel than the configuration at ID10 where the PSI Eiger 500k is about 5.3 m from the sample. In order to

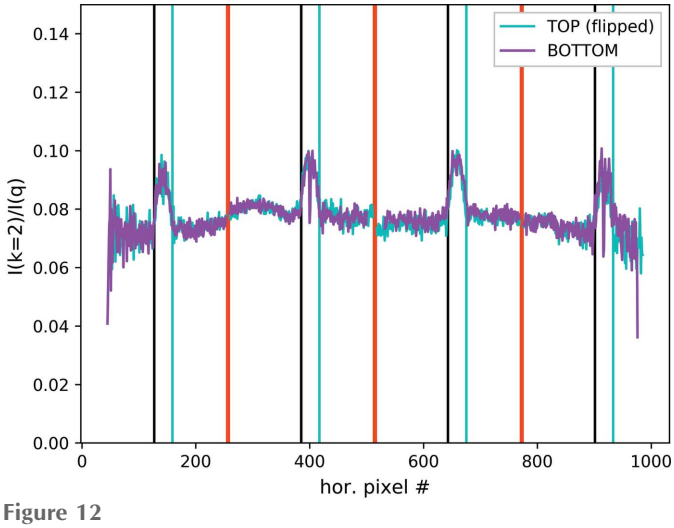

Figure 12
Fraction of the incoming intensity, which is registered as double-photon events. The data are averaged for each vertical line of the pixel and plotted as a function of horizontal position. The detector is divided into a top and a bottom half. Additionally, the horizontal direction of the top detector half is inverted, which results in a perfect overlap of both curves.

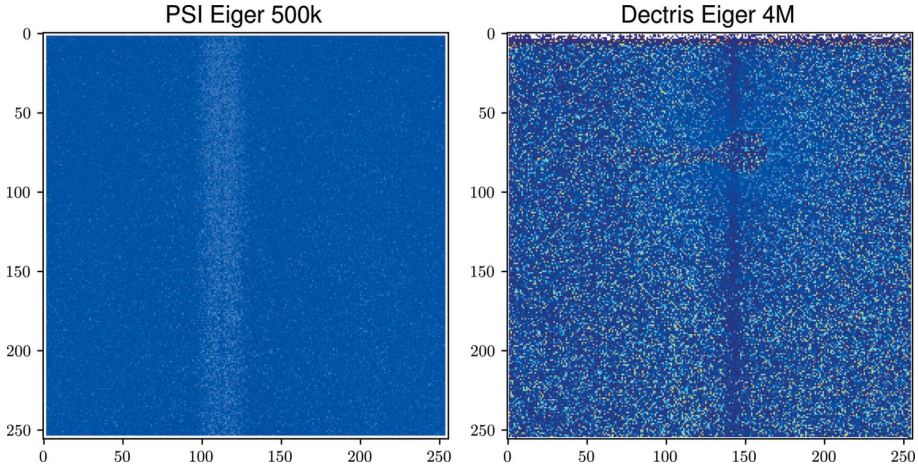

Figure 13
Fraction of double-photon events converted from the overall intensity for both detectors shown as a function of location on the single Eiger chip. The color bar is the same as in Fig. 11 (bottom). All chips are rotated so that the read-out electronics are in this representation on top of the chip. The off-stripe averages are equal to the 2κ values reported before for the two detectors.

compare the two detectors, we perform an average, overlapping all the chips of the detector, each rotated to have the same read-out orientation. The resulting conversion fraction is shown in Fig. 13.

The data for the Eiger 4M detector are more noisy, because of less flux and a smaller number of acquisitions. Therefore, a halo of the beamstop can still be seen at around the vertical pixel coordinate 75. However, we clearly obtain vertical stripe patterns for both detectors along the read-out direction. The main difference is the occurrence of a stripe with increased conversion probability for the Eiger 500k and a stripe with reduced conversion ratios in the case of the Eiger 4M. Both regions were additionally masked for the previous and following analysis, in order to evaluate only regions of the detector where the conversion probability can be assumed to be nearly constant for each pixel.

5. Colloidal dynamics obtained from XSVS

We will demonstrate that, after correcting the artificial double-photon counts, the Eiger detector can be used for XSVS experiments. We use 100 nm silica particles suspended in a water–glycerol mixture and measure speckle pattern with exposure times from 10 µs to 100 ms. Additionally, conventional XPCS measurements are conducted within the same experimental configuration, using the PSI 500k module with 22 kHz frame rate in 4-bit mode. These measurements have an exposure time of 36 µs and a latency time of 10 µs, which gives the first data point for XPCS at $t = 46$ µs. The results are shown for three q-bins in Fig. 14. The dot–dashed and dashed lines for the XPCS and XSVS experiment follow equation (2) and equation (6), respectively. For better visualization, the figure is shown with a logarithmic y scale. The corresponding plot with a conventional, linear y scale is shown in the supporting information.

The green data points correspond to the uncorrected and the black data points to the corrected contrast values. For longer exposure times, no difference between the corrected and uncorrected data is visible. A decay of β can be noted, which originates from the sample dynamics and is in line with the expected dynamics of this sample (dashed line). However, towards shorter exposure times and correspondingly smaller $\langle k \rangle$, an increase of the uncorrected data can be observed. This dependence of β on T originates from the artificial increase of double-photon events previously described. After correcting for this effect, the data points superimpose very well with the expected values.

It is evident that the uncorrected data shown in Fig. 14 can be falsely interpreted as a double decay, especially when normalized contrast values are discussed. As in general $T \propto \langle k \rangle$, this can be interpreted as sample dynamics $\beta(T)$, whereas in fact it is

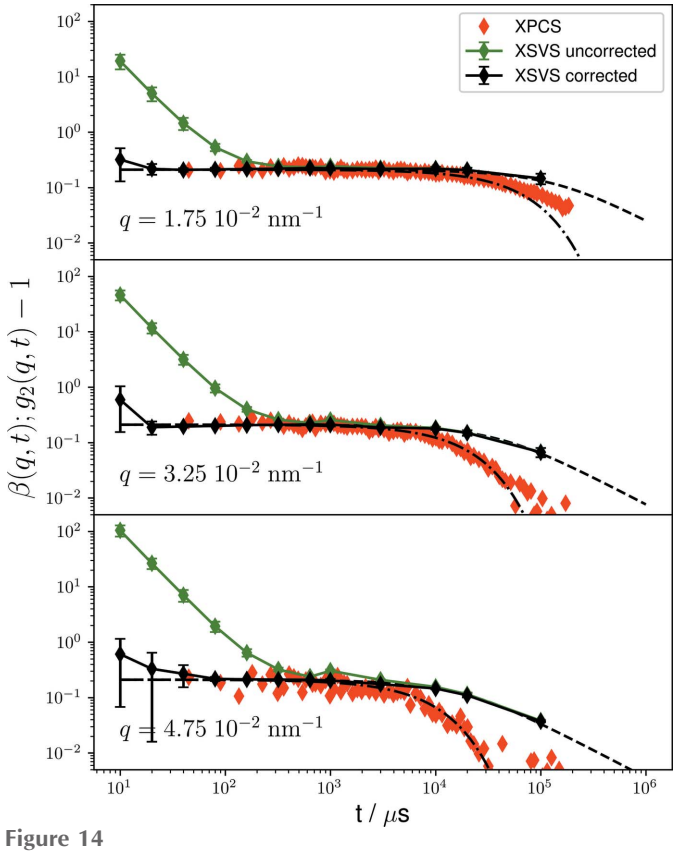

Figure 14
XPCS and XSVS measurements on 100 nm silica particles at q values of 1.75×10^{-2}, 3.25×10^{-2} and 4.75×10^{-2} nm^{-1}. The green data points correspond to the uncorrected and the black data points to the corrected XSVS results. The red data points show the XPCS results. The dot–dashed and dashed lines for the XPCS and XSVS experiment follow equation (2) and equation (6), respectively.

$\beta(\langle k\rangle)$. Therefore, a preservation of the photon-count distribution of the detector is crucial to separate contrast decays which stem from the sample dynamics and artificial effects which are detector related.

6. Conclusion

We characterized the single-photon-counting characteristics of the Eiger detector chip in terms of an X-ray speckle visibility analysis in the low-intensity regime. A systematic conversion of single-photon counts into artificial double-photon counts was observed. The most likely conversion scheme was identified as a merging effect, where two single pixels, which both should count one photon, are converted into one pixel registering two photons and one pixel registering zero photons. Characterizing the probability of this conversion on a single pixel level, a stripe-like pattern was identified on each chip for both detectors, which coincides with the read-out architecture of the chip. However, the conversion of intensity into two-photon events was found on the entire chip and is not limited to the stripe regions.

Because of the very low intensity used in the experiment, it is unlikely that the observed photon merging effect originates from a physical cross talk between neighboring pixels. A mean intensity of $\langle k\rangle = 10^{-3}$ means that one photon is registered on average in an area of 1000 pixels. The probability that two photons impinge on a neighboring pixel is therefore very small. Additionally, this should result in a dependence of κ on $\langle k\rangle$. However, κ was found to be independent of $\langle k\rangle$.

The occurrence of a stripe-like pattern along the read-out direction might hint at the read-out process being the source of the miscounting. In fact, a high level of parallel read-out is a specific feature of the Eiger detector (Dinapoli *et al.*, 2011), which might promote such an effect. For example, eight-pixel columns are grouped at the chip periphery into independent *supercolumns*. The beginning and end of the stripe patterns found in Fig. 12 coincide with the border between such supercolumns. However, the miscounting still occurs when changing the read-out mode from parallel to non-parallel (see the supporting information), which should also result in differences between the two detector modules.

The influence of the single-pixel deadtime due to pileup can most likely be excluded. The deadtime of the Eiger chip was reported to be in the range 150–300 ns (Johnson *et al.*, 2014), which is similar to the timescales obtained by the correction scheme of 330 ns [see equation (15)]. But pileup effects are typically only observed at higher count rates. Additionally, as was recently demonstrated by Zhang *et al.* (2018), a deadtime effect should result in fewer, not more, double-photon events in an XSVS experiment.

A dependence of κ on the set threshold values was found, which is described in the supporting information. However, this only shifts the level of κ, and still the miscounting persists. Another possibility is detector internal corrections, for example for pixel cross talk or pileup effects, which may be optimized for higher count regimes and disturb the counting statistics at such low count rates.

In summary, we showed that the statistical analysis of speckle pattern can serve as a sensitive tool in order to characterize the photon-counting capabilities of modern X-ray detectors. It is important to characterize detectors in the case of XSVS experiments beyond the usual linearity, flat-field and dead pixel corrections. Otherwise, the artificial increase in double-photon events might be misinterpreted as dynamics of the sample.

Acknowledgements

We acknowledge the ESRF and DESY for providing beamtime for these experiments.

References

Bandyopadhyay, R., Gittings, A., Suh, S., Dixon, P. & Durian, D. J. (2005). *Rev. Sci. Instrum.* **76**, 093110.
Carnis, J., Cha, W., Wingert, J., Kang, J., Jiang, Z., Song, S., Sikorski, M., Robert, A., Gutt, C., Chen, S.-W., Dai, Y., Ma, Y., Guo, H., Lurio, L. B., Shpyrko, O., Narayanan, S., Cui, M., Kosif, I., Emrick, T., Russell, T. P., Lee, H. C., Yu, C. J., Grübel, G., Sinha, S. K. & Kim, H. (2014). *Sci. Rep.* **4**, 6017.
Casanas, A., Warshamanage, R., Finke, A. D., Panepucci, E., Olieric, V., Nöll, A., Tampé, R., Brandstetter, S., Förster, A., Mueller, M., Schulze-Briese, C., Bunk, O. & Wang, M. (2016). *Acta Cryst.* D**72**, 1036–1048.
Chushkin, Y., Zontone, F., Lima, E., De Caro, L., Guardia, P., Manna, L. & Giannini, C. (2014). *J. Synchrotron Rad.* **21**, 594–599.
David, C., Karvinen, P., Sikorski, M., Song, S., Vartiainen, I., Milne, C., Mozzanica, A., Kayser, Y., Diaz, A., Mohacsi, I., Carini, G. A., Herrmann, S., Färm, E., Ritala, M., Fritz, D. M. & Robert, A. (2015). *Sci. Rep.* **5**, 7644.
Decker, F.-J., Akre, R., Brachmann, A., Ding, Y., Dowell, D., Emma, P. J., Fisher, A., Frisch, J., Gilevich, S., Hering, Ph., Huang, Z., Iverson, R. H., Loos, H., Messerschmidt, M., Nuhn, H.-D., Ratner, D. F., Schlotter, W. F., Smith, T. J., Turner, J. L., Welch, J. J., White, W. E. & Wu, J. (2010). *Proceedings of the 32nd International Free Electron Laser Conference (FEL2010)*, 23–27 August 2010, Malmo, Sweden, pp. 467–470. WEPB33.
Dinapoli, R., Bergamaschi, A., Henrich, B., Horisberger, R., Johnson, I., Mozzanica, A., Schmid, E., Schmitt, B., Schreiber, A., Shi, X. & Theidel, G. (2011). *Nucl. Instrum. Methods Phys. Res. A*, **650**, 79–83.
Falus, P., Lurio, L. B. & Mochrie, S. G. J. (2006). *J. Synchrotron Rad.* **13**, 253–259.
Goodman, J. (1985). *Statistical Optics.* New York: Wiley.
Grübel, G., Stephenson, G., Gutt, C., Sinn, H. & Tschentscher, T. (2007). *Nucl. Instrum. Methods Phys. Res. B*, **262**, 357–367.
Gutt, C., Stadler, L.-M., Duri, A., Autenrieth, T., Leupold, O., Chushkin, Y. & Grübel, G. (2009). *Opt. Express*, **17**, 55–61.
Hirano, T., Osaka, T., Morioka, Y., Sano, Y., Inubushi, Y., Togashi, T., Inoue, I., Matsuyama, S., Tono, K., Robert, A., Hastings, J. B., Yamauchi, K. & Yabashi, M. (2018). *J. Synchrotron Rad.* **25**, 20–25.
Hoshino, T., Kikuchi, M., Murakami, D., Harada, Y., Mitamura, K., Ito, K., Tanaka, Y., Sasaki, S., Takata, M., Jinnai, H. & Takahara, A. (2012). *J. Synchrotron Rad.* **19**, 988–993.
Hruszkewycz, S. O., Sutton, M., Fuoss, P. H., Adams, B., Rosenkranz, S., Ludwig, K. F., Roseker, W., Fritz, D., Cammarata, M., Zhu, D., Lee, S., Lemke, H., Gutt, C., Robert, A., Grübel, G. & Stephenson, G. B. (2012). *Phys. Rev. Lett.* **109**, 185502.
Inoue, I., Shinohara, Y., Watanabe, A. & Amemiya, Y. (2012). *Opt. Express*, **20**, 26878–26887.

Johnson, I., Bergamaschi, A., Billich, H., Cartier, S., Dinapoli, R., Greiffenberg, D., Guizar-Sicairos, M., Henrich, B., Jungmann, J., Mezza, D., Mozzanica, A., Schmitt, B., Shi, X. & Tinti, G. (2014). *J. Instrum.* **9**, C05032.

Johnson, I., Bergamaschi, A., Buitenhuis, J., Dinapoli, R., Greiffenberg, D., Henrich, B., Ikonen, T., Meier, G., Menzel, A., Mozzanica, A., Radicci, V., Satapathy, D. K., Schmitt, B. & Shi, X. (2012). *J. Synchrotron Rad.* **19**, 1001–1005.

Lehmkühler, F., Kwaśniewski, P., Roseker, W., Fischer, B., Schroer, M. A., Tono, K., Katayama, T., Sprung, M., Sikorski, M., Song, S., Glownia, J., Chollet, M., Nelson, S., Robert, A., Gutt, C., Yabashi, M., Ishikawa, T. & Grübel, G. (2015). *Sci. Rep.* **5**, 17193.

Li, L., Kwaśniewski, P., Orsi, D., Wiegart, L., Cristofolini, L., Caronna, C. & Fluerasu, A. (2014). *J. Synchrotron Rad.* **21**, 1288–1295.

Lu, W., Friedrich, B., Noll, T., Zhou, K., Hallmann, J., Ansaldi, G., Roth, T., Serkez, S., Geloni, G., Madsen, A. & Eisebitt, S. (2018). *Rev. Sci. Instrum.* **89**, 063121.

Lu, W., Noll, T., Roth, T., Agapov, I., Geloni, G., Holler, M., Hallmann, J., Ansaldi, G., Eisebitt, S. & Madsen, A. (2016). *AIP Conf. Proc.* **1741**, 030010.

Möller, J., Chushkin, Y., Prevost, S. & Narayanan, T. (2016). *J. Synchrotron Rad.* **23**, 929–936.

Narayanan, T., Sztucki, M., Van Vaerenbergh, P., Léonardon, J., Gorini, J., Claustre, L., Sever, F., Morse, J. & Boesecke, P. (2018). *J. Appl. Cryst.* **51**, 1511–1524.

Osaka, T., Hirano, T., Morioka, Y., Sano, Y., Inubushi, Y., Togashi, T., Inoue, I., Tono, K., Robert, A., Yamauchi, K., Hastings, J. B. & Yabashi, M. (2017). *IUCrJ*, **4**, 728–733.

Osaka, T., Hirano, T., Sano, Y., Inubushi, Y., Matsuyama, S., Tono, K., Ishikawa, T., Yamauchi, K. & Yabashi, M. (2016). *Opt. Express*, **24**, 9187–9201.

Perakis, F., Camisasca, G., Lane, T. J., *sp*äh, A., Wikfeldt, K. T., Sellberg, J. A., Lehmkühler, F., Pathak, H., Kim, K. H., Amann-Winkel, K., Schreck, S., Song, S., Sato, T., Sikorski, M., Eilert, A., McQueen, T., Ogasawara, H., Nordlund, D., Roseker, W., Koralek, J., Nelson, S., Hart, P., Alonso-Mori, R., Feng, Y., Zhu, D., Robert, A., Grübel, G., Pettersson, L. G. M. & Nilsson, A. (2018). *Nat. Commun.* **9**, 1917.

Radicci, V., Bergamaschi, A., Dinapoli, R., Greiffenberg, D., Henrich, B., Johnson, I., Mozzanica, A., Schmitt, B. & Shi, X. (2012). *J. Instrum.* **7**, C02019.

Roseker, W., Franz, H., Schulte-Schrepping, H., Ehnes, A., Leupold, O., Zontone, F., Lee, S., Robert, A. & Grübel, G. (2011). *J. Synchrotron Rad.* **18**, 481–491.

Roseker, W., Franz, H., Schulte-Schrepping, H., Ehnes, A., Leupold, O., Zontone, F., Robert, A. & Grübel, G. (2009). *Opt. Lett.* **34**, 1768–1770.

Roseker, W., Hruszkewycz, S., Lehmkühler, F., Walther, M., Schulte-Schrepping, H., Lee, S., Osaka, T., Strüder, L., Hartmann, R., Sikorski, M., Song, S., Robert, A., Fuoss, P. H., Sutton, M., Stephenson, G. B. & Grübel, G. (2018). *Nat. Commun.* **9**, 1704.

Sakamoto, J., Ohwada, K., Ishino, M., Mizuki, J., Ando, M. & Namikawa, K. (2017). *J. Synchrotron Rad.* **24**, 95–102.

Seaberg, M. H., Holladay, B., Lee, J. C. T., Sikorski, M., Reid, A. H., Montoya, S. A., Dakovski, G. L., Koralek, J. D., Coslovich, G., Moeller, S., Schlotter, W. F., Streubel, R., Kevan, S. D., Fischer, P., Fullerton, E. E., Turner, J. L., Decker, F.-J., Sinha, S. K., Roy, S. & Turner, J. J. (2017). *Phys. Rev. Lett.* **119**, 067403.

Shpyrko, O. G. (2014). *J. Synchrotron Rad.* **21**, 1057–1064.

Sun, Y., Decker, F.-J., Turner, J., Song, S., Robert, A. & Zhu, D. (2018). *J. Synchrotron Rad.* **25**, 642–649.

Verwohlt, J., Reiser, M., Randolph, L., Matic, A., Medina, L. A., Madsen, A., Sprung, M., Zozulya, A. & Gutt, C. (2018). *Phys. Rev. Lett.* **120**, 168001.

Westermeier, F., Autenrieth, T., Gutt, C., Leupold, O., Duri, A., Menzel, A., Johnson, I., Broennimann, C. & Grübel, G. (2009). *J. Synchrotron Rad.* **16**, 687–689.

Zhang, Q., Dufresne, E. M., Grybos, P., Kmon, P., Maj, P., Narayanan, S., Deptuch, G. W., Szczygiel, R. & Sandy, A. (2016). *J. Synchrotron Rad.* **23**, 679–684.

Zhang, Q., Dufresne, E. M., Narayanan, S., Maj, P., Koziol, A., Szczygiel, R., Grybos, P., Sutton, M. & Sandy, A. R. (2018). *J. Synchrotron Rad.* **25**, 1408–1416.

Zhu, D., Sun, Y., Schafer, D. W., Shi, H., James, J. H., Gumerlock, K. L., Osier, T. O., Whitney, R., Zhang, L., Nicolas, J., Smith, B., Barada, A. H. & Robert, A. (2017). *Proc. SPIE*, **10237**, 102370R.

Zinn, T., Homs, A., Sharpnack, L., Tinti, G., Fröjdh, E., Douissard, P.-A., Kocsis, M., Möller, J., Chushkin, Y. & Narayanan, T. (2018). *J. Synchrotron Rad.* **25**, 1753–1759.

Zozulya, A. V., Bondarenko, S., Schavkan, A., Westermeier, F., Grübel, G. & Sprung, M. (2012). *Opt. Express*, **20**, 18967–18976.